

Effects of particle size of mono-disperse granular flows impacting a rigid barrier

Yifei Cui¹ · Clarence E. Choi^{1,2} · Luis H. D. Liu¹ · Charles W. W. Ng¹

Received: 20 June 2017 / Accepted: 5 January 2018 / Published online: 25 January 2018
© Springer Science+Business Media B.V., part of Springer Nature 2018

Abstract Understanding the interaction between complex geophysical flows and barriers remains a critical challenge for protecting infrastructure in mountainous regions. The scientific challenge lies in understanding how grain stresses in complex geophysical flows become manifested in the dynamic response of a rigid barrier. A series of physical flume tests were conducted to investigate the influence of varying the particle diameter of mono-dispersed flows on the impact kinematics of a model rigid barrier. Particle sizes of 3, 10, 23 and 38 mm were investigated. Physical tests results were then used to calibrate a discrete element model for carrying out numerical back-analyses. Results reveal that aside from considering bulk characteristics of the flow, such as the average velocity and bulk density, the impact load strongly depends on the particle size. The particle size influences the degree of grain inertial stresses which become manifested as sharp impulses in the dynamic response of a rigid barrier. Impact models that only consider a single impulse using the equation of elastic collision warrant caution as a cluster of coarse grains induce numerous impulses that can exceed current design recommendations by several orders of magnitude. Although these impulses are transient, they may induce local structural damage. Furthermore, the equation of elastic collision should be adopted when the normalized particle size with the flow depth, δ/h , is larger than 0.9 for Froude numbers less than 3.5.

✉ Clarence E. Choi
ceclare@ust.hk

Yifei Cui
yifeicui@ust.hk

Luis H. D. Liu
hlhlaq@connect.ust.hk

Charles W. W. Ng
cecwwng@ust.hk

¹ The Department of Civil and Environmental Engineering, Hong Kong University of Science and Technology, Clear Water Bay, Kowloon, Hong Kong, China

² The HKUST Jockey Club Institute for Advanced Study, Hong Kong, China

Keywords Geophysical flows · Rigid barrier · Impact · Discrete element method · Physical flume modelling

1 Introduction

A fundamental understanding of the dynamic loading of geophysical flows against structures is crucial for estimating loading on protection structures. However, a fundamental understanding has been hindered by the poor temporal predictability of natural debris flows (Jakob and Hungr 2005). To tackle this scientific challenge, researchers have monitored the impact of natural debris flows (Hürlimann et al. 2003; Hu et al. 2011; Berger et al. 2011) and carried out large-scale experiments (DeNatale et al. 1999; Bugnion et al. 2012). However, results are difficult to interpret or generally unreproducible given the idiosyncrasies of the natural settings and the materials involved (Iverson 1997, 2015; Iverson and George 2014). This limits the extent to which the impact of geophysical flows on structures can be understood. Other limitations of field monitoring include an undefined flow properties and the inclusion of large boulders. Given these uncontrollable factors, field monitoring and large-scale tests cannot easily provide a fundamental understanding of the mechanisms of interaction between debris flows and rigid barriers.

The dynamic loading characteristics of dry granular flow on obstacles have been investigated for barriers (Zanuttigh and Lamberti 2006; Hauksson et al. 2007; Moriguchi et al. 2009; Speerli et al. 2010; Brighenti et al. 2013; Ashwood and Hungr 2016) and baffles (Choi 2013; Choi et al. 2014a; Ng et al. 2014; Choi and Law 2015). In these studies, the key impact mechanisms such as the formation of dead zones (Chu et al. 1995; Faug et al. 2002; Gray et al. 2003) and run-up (Mancarella and Hungr 2010; Choi and Law 2015) were revealed. Ng et al. (2016) and Song et al. (2017) linked the observed mechanisms with the dynamic impact response on rigid and flexible barriers using the geotechnical centrifuge. Song et al. (2017) further reported that dead zones are instrumental in redirecting momentum vertically along the barrier as run-up. This, in turn, reduces the loading at the top of the barrier. Also, dead zones contribute static loading during the impact process which augments the impact pressure.

Choi et al. (2015a, b) studied the influence of grain stresses in mono-disperse flows on the mechanisms of impact by comparing the behaviour of dry granular flow and pure water. Results revealed that frictional flows dominated by grain contact friction stresses develop a pileup mechanism. In a pileup mechanism, granular material progressively accumulates at the base of the barrier in layers and the run-up height against the barrier is suppressed by the rapid attenuation of energy through shearing of grains. By contrast, fluid flows, without grain stress and lower shear resistance, rapidly transfer momentum vertically along the barrier into run-up. Ng et al. (2017a, b, c) further studied the run-up of mono-dispersed granular flows on a rigid barrier. The degree of grain stresses was controlled by varying the particle diameter. Findings demonstrated that larger particles exhibit pronounced saltation during impact, thus resulting in higher maximum run-up heights. Evidently, impact characteristics for granular flows are strongly influenced by grain stresses (Savage and Hutter, 1989; Sovilla et al. 2008; McArdell et al., 2007) and further investigation is required to reveal their influence on the dynamic response of barriers.

Aside from physical modelling, numerical simulations are also critical to shed insight into the mechanisms of granular flows interacting with structures. The most commonly adopted approaches for modelling debris flow are based on depth-averaged continuum

models (Savage and Hutter 1989; Hungr 1995; Lin et al. 2009; Iverson and George 2014; Brunet et al. 2017). Recently, a finite element method (FEM) continuum model allowing large nonlinear deformation was benchmarked against several laboratory and field studies (Kwan et al. 2015; Koo et al. 2016). The advantages of the FEM continuum approach include its ability to allow for large deformation and its high computational efficiency for modelling large-scale problems. However, continuum methods cannot capture the obvious discrete behaviour observed during the impact of granular flow against structures (Forterre and Pouliquen 2011; Kanungo et al. 2013; DeBruyn 2011). Furthermore, it was reported that higher peak impact forces resulted from larger particles (Jiang et al. 2015) and cluster of coarse grains (Bardou et al. 2003); thus, discrete approaches such as the discrete element method are more appropriate to study the fundamental mechanisms of impact of granular flow against structures (Teufelsbauer et al. 2009; Leonardi et al. 2014; Choi et al. 2014b; Law et al. 2015).

In this study, a series of physical flume experiments were carried out to examine the fundamental mechanisms of impact between granular flows and a rigid barrier. The physical tests were back-analysed using the discrete element method to bear insight into how grain stresses are manifested through the dynamic response of the barrier.

2 Physical flume modelling

The 6-m-long physical flume model was used to carry out the physical tests in this study (Fig. 1). The rectangular channel has a width and depth of 0.2 and 0.5 m, respectively. The storage container at the most upstream end of the physical flume has a maximum storage volume of 0.1 m³. The debris is retained behind a spring-loaded gate. The gate is secured with a magnetic lock at the base of the channel. Upon deactivation of the magnetic lock, the gate swings upwards and initiates dam break.

2.1 Flow characterization

A series of open-channel tests were carried out in this study to characterize the flows. The Froude number, N_{Fr} , dynamically characterizes the ratio of inertial to gravitational forces and governs the impact mechanism of channelized geophysical flows against barriers (Armanini et al. 2011; Choi et al. 2015a, b):

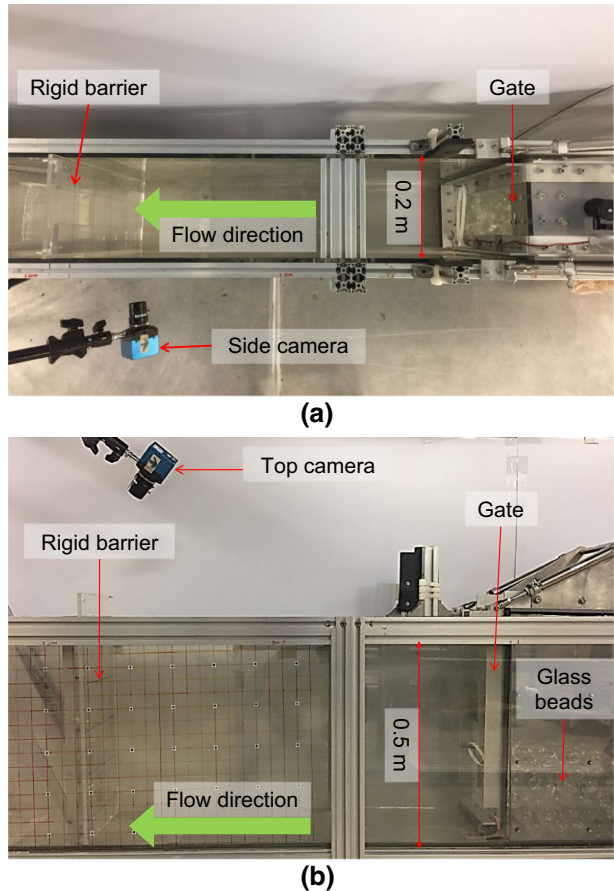
$$N_{Fr} = \frac{v_{avg}}{\sqrt{gh}} \quad (1)$$

where v_{avg} is the average flow velocity, g is the gravitational acceleration and h is the flow thickness. Grain stresses in the flows were characterized at the mesoscopic level using the Savage number (Savage 1984). The ratio of grain inertial to grain contact stresses is given as follows (Savage and Hutter 1989; Iverson 1997):

$$N_{Sav} = \frac{\dot{\gamma}^2 \delta^2}{gh \tan \theta} \quad (2)$$

where $\dot{\gamma}$ is the shear rate and is calculated by the ratio of average flow velocity to average flow thickness, δ is the particle diameter, g is gravitational acceleration, θ is the internal friction angle and h is the flow thickness.

Fig. 1 Physical flume model setup: **a** plan view; **b** side view



2.2 Instrumentation

Flow kinematics were captured using a high-speed camera (model: Mikrotron EoSens mini2), positioned at the side of the setup. The high-speed camera captures images at a resolution of 1400×1600 pixels at a sampling rate of 640 frames per second. The high-speed images enable the interpretation of velocity fields using particle image velocimetry (PIV) (White et al. 2003).

2.3 Test programme

Mono-disperse flows comprising glass spheres with diameters of 3, 10, 23 and 38 mm were used in this study. Glass spheres enable a clear definition of the characteristic grain diameter and ensure particle uniformity. Tilt tests were performed to measure the dynamic friction angles of the glass spheres (Hungar 2008; Mancarella and Hungar 2010). Tilt tests demonstrate that larger particle size have lower dynamic friction angles, aligning with the observations of Tan and Newton (1990) and Podczeczek and Mia (1996). The coefficient of

Table 1 Material properties

Parameters	Value			
Diameter (mm)	3	10	23	38
Dynamic friction angle (°)	17.8	16.6	11.6	11.6
Density (kg/m ³)	2550	2550	2550	2550
Initial bulk density (kg/m ³)	1620	1611	1583	1510
Coefficient of restitution (kg/m ³)	0.75	0.77	0.84	0.76
Young’s modulus (GPa)	60	60	60	60
Poisson ratio	0.25	0.25	0.25	0.25

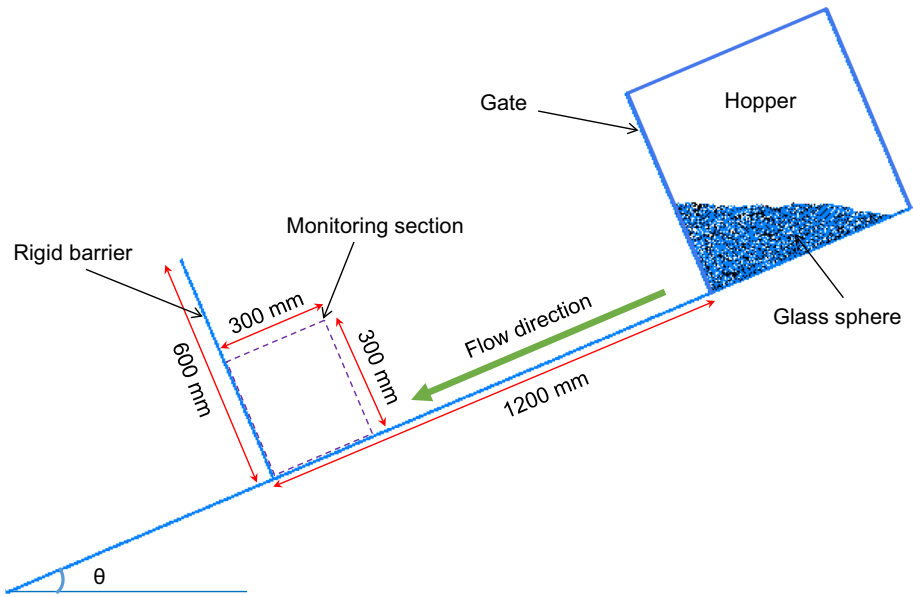


Fig. 2 Side view of numerical model setup

restitution is measured by the rebound height of a glass sphere when dropped relative to the flume base. A summary of the material properties is given in Table 1.

The channel inclination was varied to adjust N_{Fr} of the flow before impacting the model rigid barrier. To characterize N_{Fr} and N_{Sav} of the flows, control tests without a model rigid barrier installed in the channel were carried out for each combination of particle size and channel inclination. Similarly, tests were conducted with a rigid barrier installed within the channel to study the impact mechanism (Fig. 2b). A summary of the test programme is given in Table 2.

2.4 Model setup and modelling procedures

A transparent acrylic rigid barrier with a thickness, width and height of 10, 200 and 600 mm, respectively, was installed orthogonally in the channel at a distance of 1200 mm from the gate. The storage container gate was then secured using a magnetic lock and a

Table 2 Test programme

Test type	Test ID	Channel inclination angle (°)	Particle diameter (mm)
Free flow (without barrier)	F10-3	10	3
	F10-10	10	10
	F10-23	10	23
	F10-38	10	38
	F30-3	30	3
	F30-10	30	10
	F30-23	30	23
	F30-38	30	38
Barrier (with barrier)	B10-3	10	3
	B10-10	10	10
	B10-23	10	23
	B10-38	10	38
	B30-3	30	3
	B30-10	30	10
	B30-23	30	23
	B30-38	30	38

hydraulic system was used to open the gate. The granular assembly was then prepared in the storage container. An overhead crane was used to incline the flume to the desired inclination. Dam break was initiated by deactivating the magnetic lock at the base of the channel. The swinging gate was retained at its highest point of ascent to prevent it from obstructing the flow from the storage container.

3 Discrete element method (DEM)

The DEM was adopted to back-analyse the physical flume experiments carried out in this study. The DEM is used in solving many geotechnical engineering problems recently such as soil consolidation (Cui et al. 2017a, b), soil erosion (Tang et al. 2017) and landslide-induced debris flow (Yuan et al. 2015a, b). The software package Particle Flow Code in two dimensions was used (PFC^{2D}5.0) (Itasca 2014). The DEM has been widely adopted for studying geophysical flows (Zhou and Sun 2013; Zhou et al. 2015; Ng et al. 2017a, b, c). In DEM, the granular assembly is discretized into individual elements. At contacts between rigid elements, a stiffness model is used to relate the contact force to the overlapping of elements (Potyondy and Cundall 2004). Finite displacements are calculated based on Newton's laws of motion. The DEM 2D analysis is used in studying the mechanism of landslide deposition (Liu and Koyi 2013; Zhou et al. 2013; Feng et al. 2017) and, recently, debris–barrier interaction (Valentino et al. 2008; Salciarini et al. 2010). In 2D analysis, elements are treated as discs rather than particles. The limitations of 2D DEM have been highlighted by Kang (2016); these include: (1) side wall effects enhanced friction and shape of the flow front; (2) momentum transfer in the lateral direction is not considered. However, the obvious advantage of two-dimensional simulations lies in the greatly reduced number of elements in the computational domain, thereby reducing the computational time (Fleischmann et al. 2011).

3.1 Calibration and input parameters

The discrete elements have a density of 2550 kg/m³ (Ng et al. 2017a, b, c). An average coefficient of restitution of 0.78 was used based on drop tests in the laboratory (Table 3). The coefficient of friction between the discrete elements was measured from laboratory direct shear test and set as 0.7 (Chiou 2005; Teufelsbauer et al. 2011; Law et al. 2015). The discrete element and interface friction coefficient was measured by using tilting tests referring to Pudasaini and Hutter (2007), Mancarella and Hungr (2010), Jiang and Towhata (2013). The details of above two tests are mentioned in supplemented material in “Appendix 2”. The inter-element friction coefficient was set as 0.36 (Ng et al. 2017a, b, c). The stiffness of 1 × 10⁸ N/m (both normal and shear) for elements, channel walls and rigid deflector was adopted (Law et al. 2015). A summary of the input parameters adopted is given in Table 3.

3.2 Numerical model setup

The numerical model is geometrically similar to the physical model tests (Fig. 2). The storage container, channel walls and barrier are modelled as planar rigid elements. A linear contact model was adopted, consisting of a linear spring dashpot. Impact kinematics and dynamics are measured using a monitoring section, as shown in Fig. 2. The length and width of the monitoring section is 300 mm, respectively.

3.3 Numerical modelling procedure

Elements were generated in the storage container to a target mass of 20 kg. The total number of elements *N* is calculated as follows:

$$N = \frac{M_T}{M_p} \tag{3}$$

where *M_T* is the total weight of sample which is equal to 20 kg, *M_p* is the mass of the single element and *ρ* is the density of each element from Table 3. By considering the elements in PFC^{2D} analysis as discs with radius *r* and height *h* equal to channel width (0.2 m), the mass of the single cylinder can be calculated as follows:

$$M_p = \rho V_p = \rho(\pi r^2 h) \tag{4}$$

Table 3 DEM input parameters

Parameters	Values
Wall normal stiffness (N/m)	1 × 10 ⁸
Wall normal-to-shear stiffness ratio (dimensionless)	1
Element normal stiffness (N/m)	1 × 10 ⁸
Element normal-to-shear stiffness ratio (dimensionless)	1
Element radius (mm)	3; 10; 23; 38
Element density (kg/m ³)	2550
Inter-element friction coefficient (dimensionless)	0.36
Interface-element friction coefficient (dimensionless)	0.4
Gravitational acceleration (m/s ²)	9.81
Coefficient of restitution (dimensionless)	0.78

A gravitational acceleration of 9.81 m/s^2 was applied to the computational domain and elements were allowed to free fall into the storage container until the ratio of average unbalanced force to the average contact forces converged to less than 1% difference (Cui et al. 2016). The storage container gate was then deleted to simulate dam break, and discrete elements were allowed to flow down the channel and impact the rigid barrier.

4 Results and interpretation

4.1 Numerical flow characterization

Flows were characterized in channels that were unobstructed. Results are summarized in Table 4. Two Froude numbers were characterized based on the channel inclination. All the subsequent data interpretation will be based on these two types of fluid flow.

4.2 Run-up

For tests with a rigid barrier installed in the channel, the impact kinematics for normalized diameters (δ/h) of 0.43 (test B30-10) were compared between the computed results and the observed phenomenon at the highest run-up height for a channel inclination of 30° . The flow front arrives just upstream of the barrier at $t = 0 \text{ s}$ from the right (Fig. 3a). The maximum velocity deduced using PIV analysis is 4 m/s . A collisional flow front impacts the barrier, and particles are observed to run up along the vertical face of the barrier. The maximum velocity reduced by 34%. Near the leading-edge of the run-up front, saltation of particles is observed at the barrier face in both numerical and experimental results (Fig. 3b). Velocity vectors from PIV analysis indicate the change in particle trajectory after collision, and particles are also observed falling back towards the channel. The maximum velocity vector shows a rapid attenuation in terms of kinetic energy of the flow after impact in both PIV and DEM analysis. During the impact process, granular material deposits, namely dead zones, at the base of the barrier. Subsequent granular flow continues to impact the ramp-like dead zone in layers (Fig. 3c). Eventually, the granular mass reaches a static state at about $t = 1.38 \text{ s}$. The observed mechanism is reminiscent to that described in Choi et al. (2015a, b) for dry granular material.

Table 4 Summary of simulation results

Test ID	Average flow velocity v (m/s)	Average flow depth h (m)	Particle size-to-flow depth ratio δ/h	Shear rate $\dot{\gamma}$	Froude Fr	Savage $NSav$
F10-3	0.19	0.013	0.23	14.80	4.86	0.05
F10-10	0.54	0.018	0.55	29.31	3.71	1.60
F10-23	1.01	0.034	0.68	29.62	3.07	6.78
F10-38	1.44	0.050	0.76	28.85	2.49	11.82
F30-3	2.37	0.020	0.15	117.61	7.99	1.96
F30-10	2.38	0.024	0.43	101.13	7.15	14.90
F30-23	2.51	0.045	0.51	56.09	4.60	18.45
F30-38	2.53	0.062	0.62	41.15	3.75	19.57

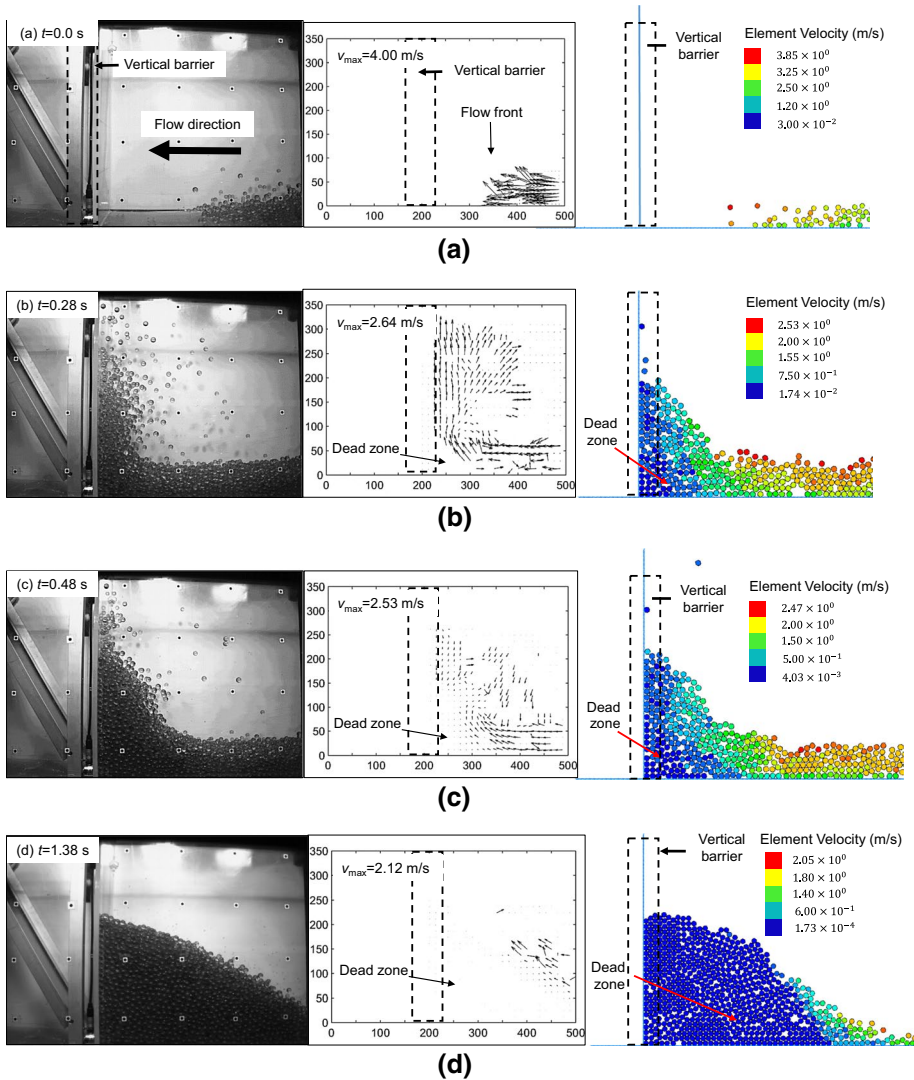


Fig. 3 Comparison of observed and computed flow dynamics (test B30-10): **a** $t = 0$ s; **b** $t = 0.28$ s; **c** $t = 0.48$ s; **d** $t = 1.38$ s

The computed maximum run-up height is noticeable lower than that measured because a mass control approach was used instead of a volume control approach. The mass of a single element in a 2D analysis is transformed from 3D by assuming a disc in 3D using Eq. 4. Therefore, the solid volume in 2D case is larger compared to that for a 3D scenario. The total number of particles calculated from 2D analysis is less than the physical tests. The disparity in the number of particles between the physical tests and simulations is most evident in the number of particles saltating during the impact process.

An additional 3D discrete element simulation, using PFC3D (Itasca 2014) was conducted in order to compare impact force time history with 2D analysis. The input

parameters and modelling procedures are parallel to those used in the 2D simulations. The detail of the comparison and discussion is described in “Appendix 1” in supplementary material at the end of the text.

4.3 Dynamic response of rigid barrier

Figure 4 shows the impact force for normalized diameters of 0.23 (Fig. 4a), 0.54 (Fig. 4b), 0.68 (Fig. 4c) and 0.76 (Fig. 4d) at a channel inclination of 10°, corresponding to an average characteristic N_{Fr} of about 3.53. The dynamic impact load is normalized by the static load acting on the barrier. To take account of the impact of hard and discrete inclusions within geophysical flows, a reference impact load based on the Hertz equation is generally adopted. The Hertz equation, for the estimation of boulder impact load F , presented by Zhang et al. (1996) is shown as follows:

$$F = K_c n \alpha^{1.5} \tag{5}$$

where K_c is load reduction factor, considered as a dimensionless number, and n and α can be calculated by the following equations:

$$n = \frac{4r_s^{0.5}}{3\pi(k_s + k_b)} \tag{6}$$

$$\alpha = \left(\frac{5m_s v_s^2}{4n} \right)^{0.4} \tag{7}$$

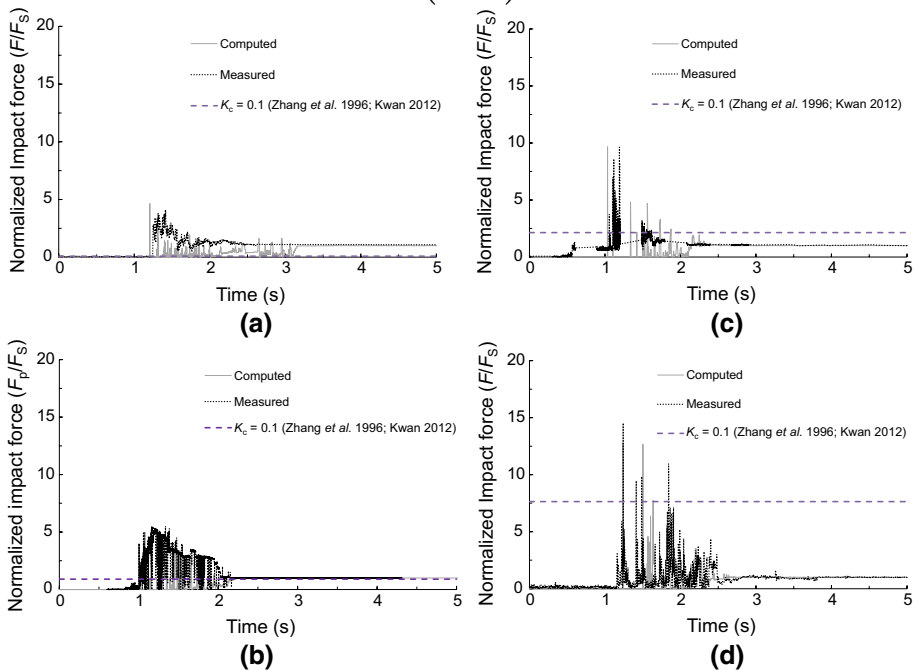


Fig. 4 Comparison between measured and computed impact load on rigid barrier (10°): **a** $\delta/h = 0.23$; **b** $\delta/h = 0.54$; **c** $\delta/h = 0.68$; **d** $\delta/h = 0.76$

where r_s is the radius of a single sphere, m_s is the mass of a single sphere, v_s is impact velocity of the sphere normal to the barrier, k_s and k_b are coefficients related to the Young’s modulus and the Poisson ratios of the sphere and barrier:

$$k_s = \frac{1 - \mu_s^2}{\pi E_s} \tag{8}$$

$$k_b = \frac{1 - \mu_b^2}{\pi E_b} \tag{9}$$

where μ_s and μ_b , and E_s and E_b are elastic moduli and Poisson ratios of glass sphere and barrier, respectively.

In the laboratory experiment, the rigid barrier was an acrylic plate, which has a Young’s modulus and a Poisson ratio of 3.2 GPa and 0.35, respectively. Meanwhile, the Young’s modulus and the Poisson ratio of glass spheres are 3.2 GPa and 0.35, respectively. All input parameters are summarized in Table 1. The Hertz equation assumes an elastic impact between a single sphere and a plane for continuous isotopic material. However, an entire granular assembly was computed in this study. The performance of the load reduction factor K_c for a granular assembly remains unclear. In the current study, K_c is taken as 0.1 for rigid barrier (Kwan 2012).

For each simulation, impulses are generated by individual elements which transfer momentum to the barrier with very short durations within 1 s. The peak dynamic-to-static load ratio for normalized diameters (δ/h) of 0.23, 0.54, 0.68 and 0.76 are about 4, 5, 10 and 14, respectively. The maximum difference between computed and measured peak normalized impact forces is 10%. The magnitude of the peak loads becomes smaller as the diameter decreases. In practice, these large impulses can be accounted for using the Hertz equation (Eq. 5). The normalized impact force from the Hertz equation is negligible for the case of normalized diameters (δ/h) of 0.23 and 0.54, indicating that considering the particle size is necessary when adopting the Hertz equation. With an increasing particle size, the normalized impact force from the Hertz equation increases and tends towards the peak impact load, as shown in Fig. 4c, d, when the normalized diameters (δ/h) of 0.68 and 0.76. This indicates that for larger particle sizes, the Hertz equation is necessary to account for the discrete nature of larger particles during impact. This further corroborates the need to consider both continuum and discrete loading from larger particles for barrier design.

Figure 5 shows the impact force profiles for normalized diameters of 0.15 (Fig. 5a), 0.43 (Fig. 5b), 0.51 (Fig. 5c) and 0.62 (Fig. 5d) at an inclination of 30° corresponding to a average characteristic N_{Fr} of about 5.8. This characteristic N_{Fr} for an inclination of 30° is higher than that of N_{Fr} for simulations carried out at an inclination of 10° because of a higher inertial component. The higher N_{Fr} is responsible for generating higher peak impulses on the barrier. More specifically, the normalized peak-to-static load ratios for normalized diameters (δ/h) of 0.15, 0.43, 0.51 and 0.62 are about 9, 11, 13 and 15 at 30°. A recurrent trend with increasing peak impulses generated with larger diameters is observed.

Figure 6a shows the effect of the normalized diameter on the load reduction factor adopted in the Hertz equation (Leroy 1985; Zhang et al. 1996; Kwan 2012). A horizontal reference line is used to show the recommended load reduction factor K_c of 0.1 as proposed by Kwan (2012) for a spherical granite boulder impacting a rigid reinforced concrete barrier. The load reduction factors in this study were back-calculated using the peak forces obtained from each numerical simulation. The load reduction factor depends on the

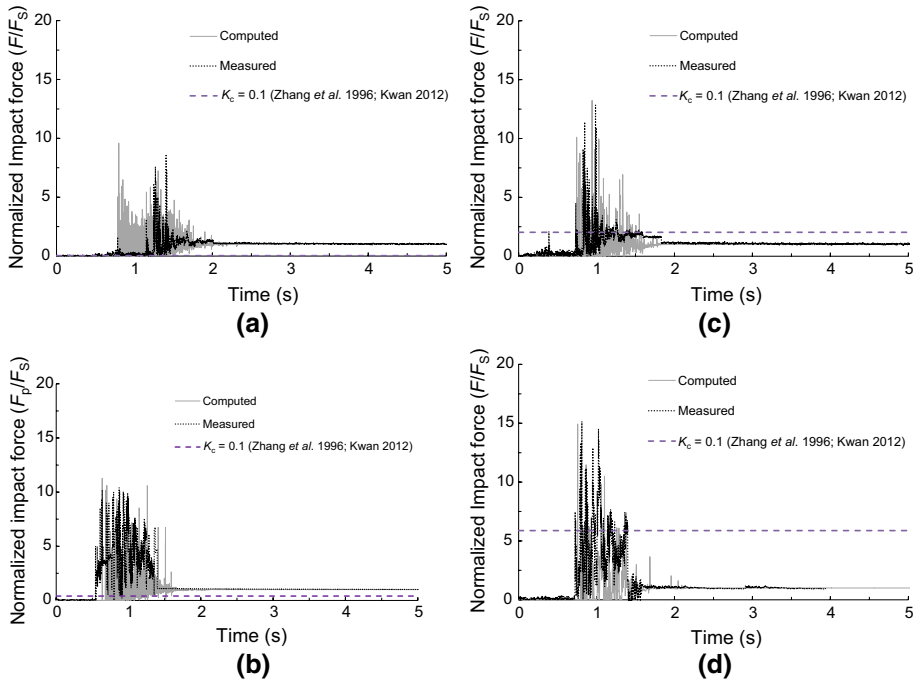


Fig. 5 Comparison between measured and computed impact load on rigid barrier (30°): **a** $\delta/h = 0.15$; **b** $\delta/h = 0.43$; **c** $\delta/h = 0.51$; **d** $\delta/h = 0.62$

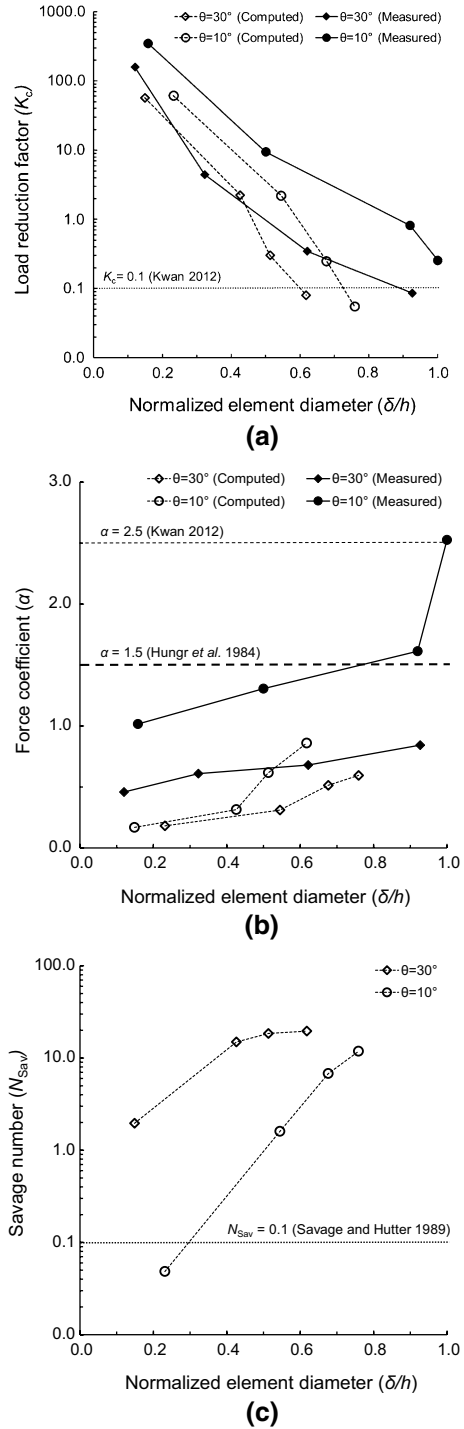
diameter of each element for both measured and computed results. As the diameter of each element increases, the load reduction factor decreases. Experimental results also show that for contact-dominated flow (channel inclination of 10 degree and $N_{Fr} = 3.5$) the load reduction factor for normalized element diameters larger than 0.9 agrees with the recommended design value, indicating that the Hertz equation (Eq. 5) is suitable for larger boulders in practical barrier design. Likewise, for the computed results, under the same Froude condition, the load reduction factor for normalized diameters larger than 0.7 agrees with the recommended design value of 0.1. The computed results show a reasonable agreement with measured results for granular flow with smaller particles ($\delta/h < 0.4$). But the discrepancy between computed and measured results increases for the granular flow with large particles ($\delta/h > 0.4$). This discrepancy is caused by the difference in impact velocity and average flow depth. In comparison with the laboratory tests, the DEM model assumes a cylinder rather than a sphere. The larger friction on the cylinder will inevitably result in smaller impact velocities.

Figure 6b shows the effect of normalized diameter on the force coefficient adopted in the momentum equation (Hungri et al. 1984; Kwan 2012). A reference impact load based on the momentum equation (VanDine 1996; Proske et al. 2011) is given as follows:

$$F = \alpha \rho v_{avg}^2 h_{avg} w \tag{10}$$

where α is the force coefficient for rigid barrier, ρ is the bulk density of the debris material, h_{avg} is the average flow depth and v_{avg} is the average flow velocity in free flow test and w is the channel width. The momentum equation assumes a uniform and dynamic impact for a

Fig. 6 Effect of normalized element diameter: **a** force coefficient from the momentum equation; **b** load reduction factor from the Hertz equation; **c** savage number



continuum of uniform density (Zhang et al. 1996; Kwan 2012; SWCB 2005). Two horizontal reference lines showing the recommended force coefficient $\alpha = 2.5$ (Kwan 2012) and $\alpha = 1.5$ (Hung et al. 1984), respectively, for a rigid barrier, are shown in comparison with numerical and experimental results. The force coefficients were back-calculated using the computed peak forces. Results demonstrate that the force coefficient is strongly dependent on both the diameter and N_{Fr} . As both the diameter and N_{Fr} increase, the force coefficient increases accordingly. All computed normalized diameters remained bounded by the momentum equation (Eq. 6) except for the normalized diameters of 1.0 case in laboratory result for inertial dominated flow condition (channel inclination angle of 30 degree and $N_{Fr} = 5.8$). This suggests that the currently recommended momentum approach and force coefficient of 2.5 may not be sufficient to cover discrete impacts.

Results further reveal that for mono-disperse flows, the particle size is a crucial consideration. This is different to existing guidelines where only the bulk characteristics of the flow, specifically the flow velocity and bulk flow density, are considered. Grain stresses characterized using the N_{Sav} (Table 4) corroborate the influence of particle size on the dynamic response on a rigid barrier. A granular assembly comprising smaller diameters has a higher degree of contact grain stresses. This enables rapid attenuation of flow energy. By contrast, larger diameters have a higher degree of inertial grain stresses that become manifested into high impulses on the rigid barrier.

Figure 6c shows that the calculated Savage number increases with the element size. Computed results show that the Savage number increases when the normalized diameter increases. This implies that granular flows with larger particles are more inertial. Results demonstrate that Savage number is also strongly dependent on N_{Fr} . For same particle size, N_{Fr} increases, while the Savage number also increases accordingly. This indicates that the granular flow condition changes to stresses dominated by grain collision. In this study, δ/h affects the flow dynamics significantly, which is in agreement with the findings of Ng et al. (2017a, b, c).

Furthermore, findings from this study suggest that contact-dominated flows are more likely to behave like a continuum, and therefore, it is more appropriate to adopt continuum-based approaches to estimate the impact load. However, geophysical flows with particles that are larger will generate impulses that may exceed the momentum equation.

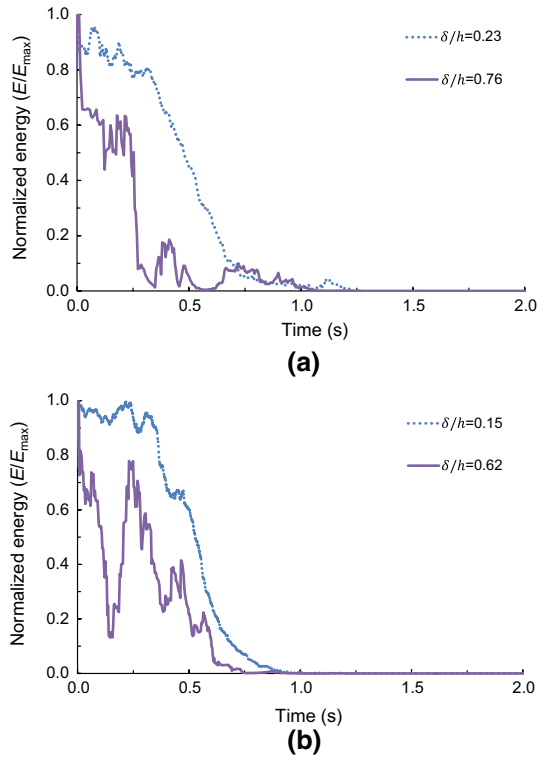
4.4 Impact energy

Figure 7 shows a comparison of the kinetic energy profiles after the initial impact for the largest and smallest normalized particle sizes in this study, specifically $\delta/h = 0.23$ and 0.76 for $N_{Fr} = 5.9$, and $\delta/h = 0.15$ and 0.62 for $N_{Fr} = 3.5$. The kinetic energy is calculated by the following equation:

$$E = \frac{1}{2} \sum_{i=1}^{i=n} m_i v_i^2 \quad (11)$$

where n is the total number of elements in the region of measurement as shown in Fig. 2, m_i is the mass of each individual element and v_i is the velocity of each individual element. The energy profiles are shown as the flow impacts the barrier. The kinetic energy is normalized by the maximum impact energy (E_{max}) of each case. A reduction in kinetic energy towards the static state is observed from each profile (Fig. 7). It is evident that for larger particle diameters, the energy drops much more rapidly compared to the smaller particles.

Fig. 7 Normalized energy dissipation profiles during impact: **a** slope inclination $\theta = 10^\circ$; **b** slope inclination $\theta = 30^\circ$



For steeper channel inclinations, a quicker energy dissipation rate is observed. This indicates that N_{Fr} has a strong influence on the rate of energy dissipation. A higher degree of fluctuation during energy dissipation process is observed in both Fig. 7a, b for larger normalized particle sizes. The reason of higher degree of fluctuation is that since the flow condition changes to grain collision stress dominated with larger normalized particle size, the higher shear rate in collision-dominated flows may result in more inertial flows that exhibit a higher degree of discrete impulses during the whole impact process, including the continuous impact of element at the tail of flow.

5 Conclusions

A series of physical flume tests were carried out and back-analysed using the discrete element method. Findings are drawn as follows:

- (a) Conventionally, only bulk characteristics, such as the average velocity and bulk density, are considered when estimating the impact load of geophysical flows. Findings show that the particle size is another important variable that warrants consideration. The particle size strongly influences the degree of grain inertial stresses which become manifested as sharp impulses on the dynamic response of a rigid barrier.

- (b) Impact models that only consider a single impulse using the Hertz equation warrant caution as a cluster of coarse grains induce numerous impulses that can exceed current design recommendations by several orders of magnitude.
- (c) The reduction factor K_c in the Hertz equation is strongly dependent on the particle size. Caution is required to ensure a conservative estimate for designing a barrier. For gravitational dominated flow ($N_{Fr} < 3.5$), it is suggested to adopt the Hertz equation when the characteristic particle size (δ/h) is larger than 0.9.
- (d) The force coefficient α in hydrodynamic model is strongly dependent on the particle size. As the particle size increases, the force coefficient increases accordingly. For inertial dominated flow ($N_{Fr} > 5.8$), fine particles (the normalized particle diameter $\delta/h < 0.5$) do not generate sharp impulses that exceed the momentum equation set forth in international guidelines. By contrast, coarser particles (the normalized particle diameter $\delta/h > 0.9$) generate sharp impulses that exceed the momentum equation.

Acknowledgements The authors are grateful for financial support from the theme-based Research Grant T22-603/15-N and the General Research Fund 16209717 provided by the Research Grants Council of the Government of Hong Kong SAR, China. The authors would like to gratefully acknowledge the support of the HKUST Jockey Club Institute for Advanced Study. The authors would also like to thank the financial support from the Natural Science Foundation of China (E090705).

Appendix 1: Comparison of numerical 2D and 3D analysis

Input parameters and modelling procedures

The 3D numerical model is geometrically similar to the physical model tests (Fig. 8). The storage container, channel walls and barrier are modelled as planar and rigid elements. A linear contact model was adopted, consisting of a linear spring dashpot. Impact kinematics and dynamics were measured along the height of the barrier. The input parameters and modelling procedures are reminiscent to those used in the 2D simulations. Each simulation included the generation of a target mass of 20 kg. The total number of elements N is calculated as follows:

$$N = \frac{M_T}{M_p} \quad (12)$$

where M_T is the total weight of sample which is equal to 20 kg, M_p is the mass of a single particle in 3D case, and can be calculated from Eq. 4:

$$M_p = \rho V_p = \rho \left(\frac{4}{3} \pi r^3 \right) \quad (13)$$

where ρ and r are the density and radius of each element, respectively.

After the generation of particles, a gravitational acceleration of 9.81 m/s² was applied to the computational domain and elements were allowed to free fall in the storage container until the ratio of average unbalanced force to the average contact forces converged was less than 1% difference (Cui et al. 2016). The storage container gate was then deleted to simulate dam break initiation mechanism to release the discrete elements downslope into the rigid barrier.

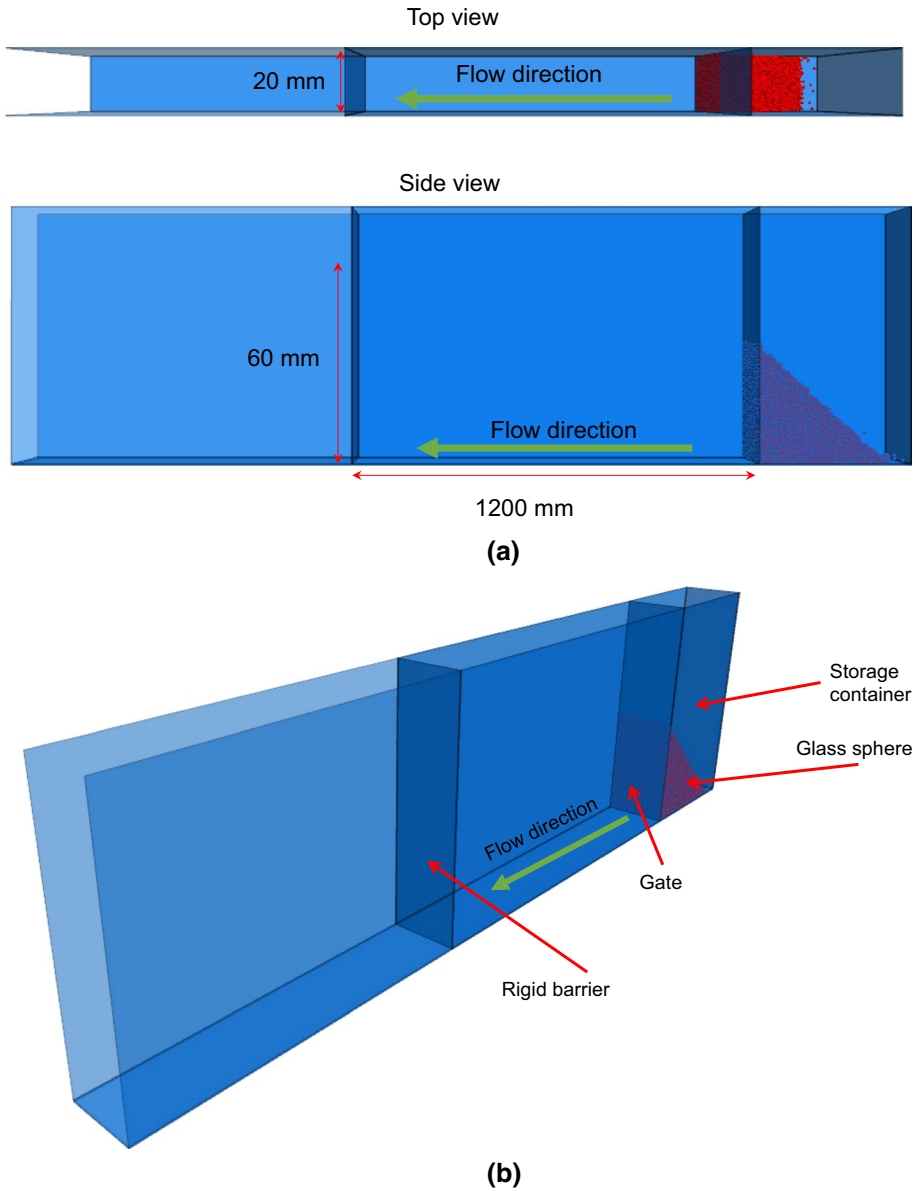


Fig. 8 3D Numerical model setup: **a** top and side view; **b** 3D view

Interpretation and discussion

Results show that for 3D simulation, the impact load exhibit a disparity of about 20% less compared to 2D simulation. The difference is attributed predominantly to side wall effects, which is the most apparent from observing the geometry of the flow fronts in both the 2D and 3D simulations. Furthermore, the 2D simulations exhibit several distinct impulses after

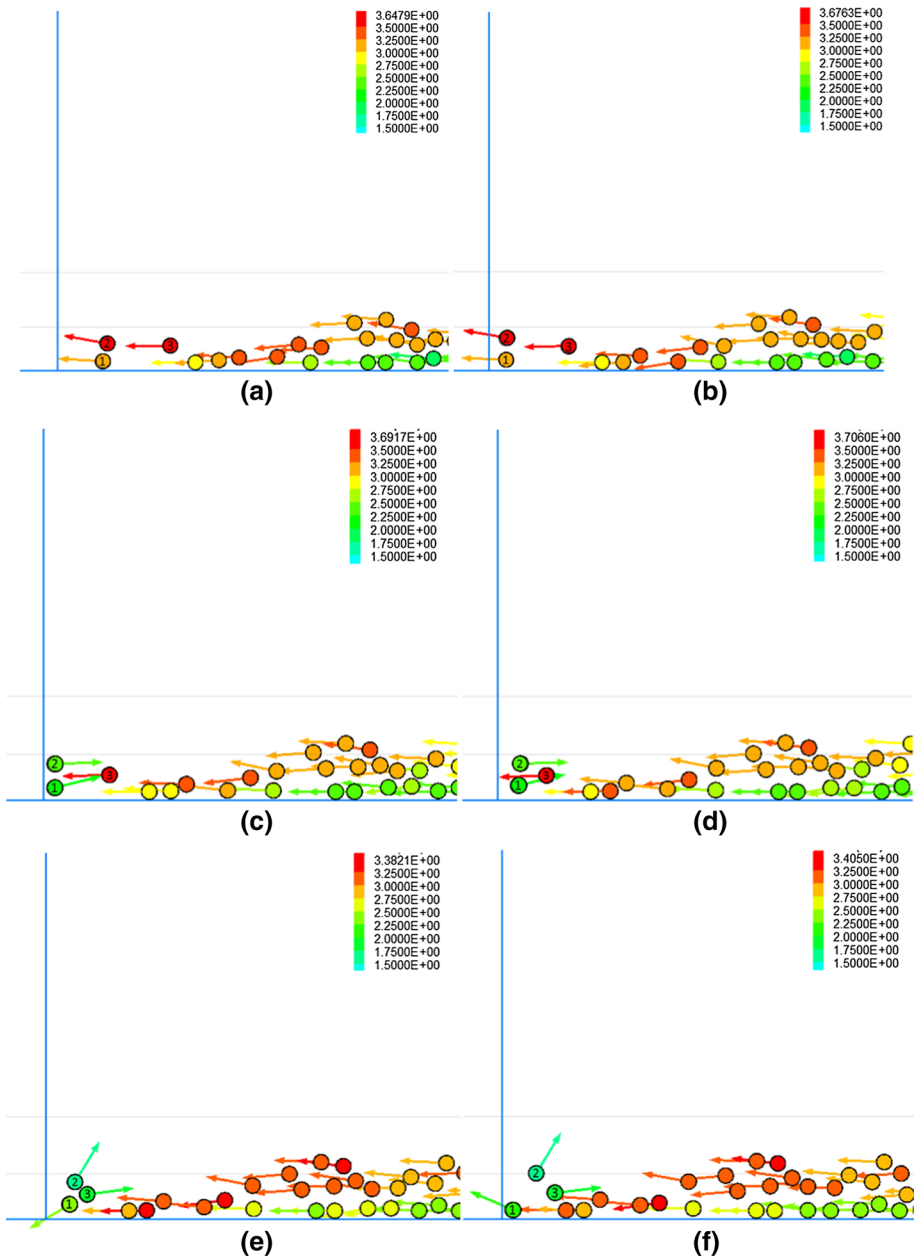


Fig. 9 Impact mechanism between first and second impact on rigid barrier (30°) when $\delta/h = 0.43$: **a** $t = 0.719$ s; **b** $t = 0.734$ s; **c** $t = 0.749$ s; **d** $t = 0.764$ s; **e** $t = 0.779$ s; **f** $t = 0.794$ s

the initial peak impulse. By contrast, the 3D simulations did not have such observation. This is because of the enhanced degree of freedom for the 3D simulations. The additional degree of freedom enhances the attenuation of flow energy in the direction perpendicular to the flow.

Fig. 10 Comparison of the impact load history on rigid barrier (30°) when $\delta/h = 0.43$

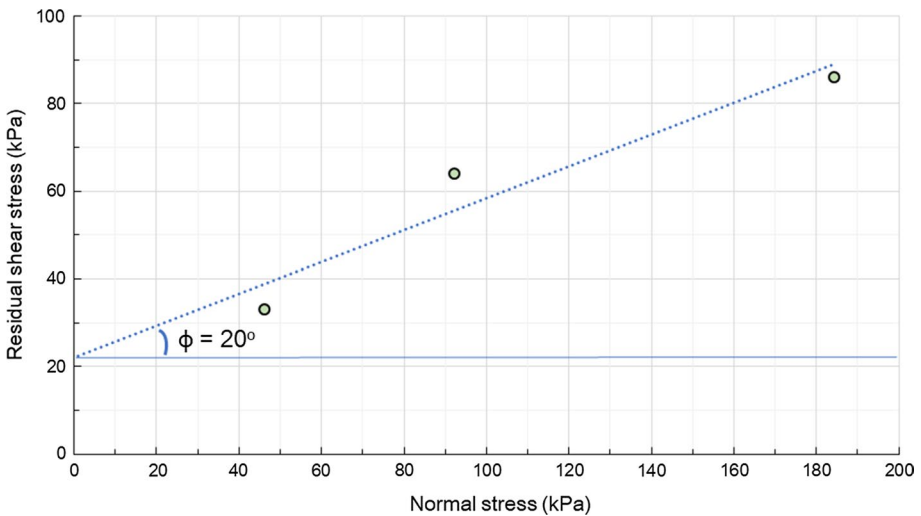
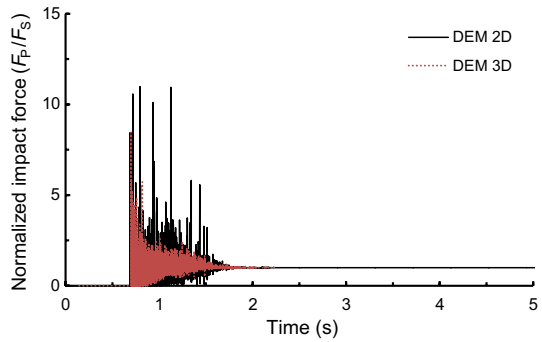


Fig. 11 Results of direct shear test on 3-mm-diameter glass sphere assembly

To further elucidate the impact mechanism pertaining to the 2D simulations, the computed flow kinematics between the first and second impacts (computational time from 0.719 s to 0.794 s) are shown in Fig. 9a–f. The arrow of each particle indicates a velocity vector. From the computed results, it is evident that two particles in particular (Particles No. 1 and No. 2) impact the rigid barrier almost simultaneously (Fig. 9a, b). After the first impact, Particles No. 1 and No. 2 rebound and collide with the incoming particles, specifically Particle No. 3 (Fig. 9c, d). After this collision, Particle No. 1 bounces back towards the barrier and induces a second impact (Fig. 9e, f).

The observed dynamics lead to two distinct impact forces as shown in Fig. 10. By contrast, this phenomenon is not as evident in the 3D simulations because a larger number of particles and greater momentum transfer in the lateral direction lead to lower impact loads for the 3D case compared to the 2D case.

Appendix 2: Calibration of frictional parameter

Before the experimental flume test, the direct shear test is carried out for glass spheres with 3 mm diameter, following the standard ASTM standard (ASTM 2011). The samples were filled in a standard shear box measuring $50.8 \times 50.8 \times 21.5$ mm (width \times length \times height), after which a constant compaction effort was applied to the samples, which brought them to a dense state and similar densities. The samples were tested at 45, 90 and 180 kPa normal stresses in a strain-controlled mode at a shear rate of 0.02 mm/min. Figure 11 shows the frictional angle for 3-mm-diameter glass sphere is 20 degree, which corresponds to the inter-element frictional coefficient of 0.36.

The interface-element frictional coefficient of the glass sphere was measured in Choi et al. (2016) by means of tilting tests referring to Pudasaini and Hutter (2007), Mancarella and Hungr (2010), Jiang and Towhata (2013). A cylindrical container of 200 mm diameter filled with granular material to a height of 100 mm was placed on the channel. The channel was inclined until the container began to slide. At this moment, the angle of the channel was recorded as the interface friction angle. The recorded angle 22 degree is then converted to interface-element frictional coefficient as 0.4 in DEM calculations.

References

- Armanini A, Larcher M, Odorizzi M (2011) Dynamic impact of a debris flow front against a vertical wall. In: Proceedings of 5th international conference on debris-flow hazards “mitigation, mechanics, prediction and assessment”, Padua, Italy
- Ashwood W, Hungr O (2016) Estimating the total resisting force in a flexible barrier impacted by a granular avalanche using physical and numerical modeling. *Can Geotech J*. <https://doi.org/10.1139/cgj-2015-0481>
- ASTM (2011) Standard test method for direct shear test of soils under consolidated drained conditions. D3080/D3080 M. West Conshohocken, PA
- Bardou E, Ancey C, Bonnard C, Vulliet L (2003) Classification of debris-flow deposits for hazard assessment in alpine areas. In 3th international conference on debris-flow hazards mitigation: mechanics, prediction, and assessment, Millpress
- Berger C, McArdell BW, Schlunegger F (2011) Sediment transfer patterns at the Illgraben catchment, Switzerland: implications for the time scales of debris flow activities. *Geomorphology* 125(3):421–432
- Brighenti R, Segalini A, Ferrero AM (2013) Debris flow hazard mitigation: a simplified analytical model for the design of flexible barriers. *Comput Geotech* 54:1–15
- Brunet M, Moretti L, Le Friant A, Mangeney A, Nieto EDF, Bouchut F (2017) Numerical simulation of the 30–45 ka debris avalanche flow of Montagne Pelée volcano, Martinique: from volcano flank collapse to submarine emplacement. *Nat Hazards* 87(2):1189–1222
- Bugnion L, McArdell B, Bartelt P, Wendeler C (2012) Measurements of hillslope debris flow impact pressure on obstacles. *Landslides* 9(2):179–187
- Chiou MC (2005) Modelling of dry granular avalanches past different obstructions: numerical simulations and laboratory analyses. Ph.D. dissertation, Technical University Darmstadt
- Choi CE (2013) Flume and discrete element investigation of granular flow mechanisms and interaction with baffles. Ph.D. thesis. Hong Kong University of Science and Technology, Hong Kong, China
- Choi CE, Law RPH (2015) Mechanisms and performance of landslide debris flow baffles. *HKIE T* 22(4):235–246
- Choi CE, Ng CWW, Song D, Kwan JSH, Shiu HYK, Ho KKS, Koo RCH (2014a) Flume investigation of landslide debris baffles. *Can Geotech J* 51(5):533–540
- Choi CE, Ng CWW, Song D, Law RPH, Kwan JSH, Ho KKS (2014b) A computational investigation of baffle configuration on the impedance of channelized debris flow. *Can Geotech J* 52(2):182–197
- Choi CE, Au-Yeung S, Ng CWW (2015a) Flume investigation of landslide granular debris and water runoff mechanisms. *Geotech Lett* 5(1):28–32
- Choi CE, Ng CWW, Au-Yeung SCH, Goodwin G (2015b) Froude scaling of landslide debris in flume modelling. *Landslides* 12(6):1197–1206

- Choi CE, Goodwin GR, Ng CWW, Cheung DKH, Kwan JSH, Pun WK (2016) Coarse granular flow interaction with slit structures. *Geotech Lett* 6(4):267–274
- Chu T, Hill G, McClung DM, Ngun R, Sherkat R (1995) Experiments on granular flows to predict avalanche runup. *Can Geotech J* 32(2):285–295
- Cui Y, Nouri A, Chan D, Rahmati E (2016) A new approach to DEM simulation of sand production. *J Petrol Sci Eng* 147:56–67
- Cui Y, Chan D, Nouri A (2017a) Discontinuum modeling of solid deformation pore-water diffusion coupling. *Int J Geomech*. [https://doi.org/10.1061/\(ASCE\)GM.1943-5622.0000903](https://doi.org/10.1061/(ASCE)GM.1943-5622.0000903)
- Cui YF, Chan D, Nouri A (2017b) Coupling of solid deformation and pore pressure for undrained deformation—a discrete element method approach. *Int J Numer Anal Meth Geomech* 41(18):1943–1961
- DeBruyn J (2011) Viewpoint: unifying liquid and granular flow. *Physics* 4:86
- DeNatale JS, Iverson RM, Major JJ, LaHusen RG, Fiegel GL, Duffy JD (1999) Experimental testing of flexible barriers for containment of debris flows. US Department of the Interior, US Geological Survey
- Faug T, Lachamp P, Naaim M (2002) Experimental investigation on steady granular flows interacting with an obstacle down an inclined channel: study of the deadzones upstream from the obstacle application to interaction between dense snow avalanches and defence structures. *Nat Hazards Earth Syst Sci* 2:187–191
- Feng Z, Lo C, Lin Q (2017) The characteristics of the seismic signals induced by landslides using a coupling of discrete element and finite difference methods. *Landslides* 14(2):661–674
- Fleischmann JA, Plesha ME, Drugan WJ (2011) Quantitative comparison of two-dimensional and three-dimensional discrete-element simulations of nominally two-dimensional shear flow. *Int J Geomech* 13(3):205–212
- Forterre Y, Pouliquen O (2011) *Granular flows. Glasses and Grains*. Springer, Basel, pp 77–109
- Gray JMNT, Tai YC, Noelle S (2003) Shock waves, dead zones and particle-free regions in rapid granular free-surface flows. *J Fluid Mech* 491:161–181
- Hauksson S, Pagliardi M, Barbolini M, Jóhannesson T (2007) Laboratory measurements of impact force of supercritical granular flow against mast-like obstacles. *Cold Reg Sci Technol* 49(1):54–63
- Hu K, Wei F, Li Y (2011) Real-time measurement and preliminary analysis of debris-flow impact force at Jiangjia Ravine, China. *Earth Surf Process Landf* 36(9):1268–1278
- Hungr O (1995) A model for the runout analysis of rapid flow slides, debris flows, and avalanches. *Can Geotech J* 32:610–623
- Hungr O (2008) Simplified models of spreading flow of dry granular material. *Can Geotech J* 45(8):1156–1168
- Hungr O, Morgan GC, Kellerhals R (1984) Quantitative analysis of debris torrent hazards for design of remedial measures. *Can Geotech J* 21(4):663–677
- Hürlimann M, Rickenmann D, Graf C (2003) Field and monitoring data of debris-flow events in the Swiss Alps. *Can Geotech J* 40(1):161–175
- Itasca, Consulting Group Inc 2014. PFC particle flow code. Ver. 5.0 Manual. Itasca, Minneapolis
- Iverson RM (1997) The physics of debris flows. *Rev Geophys* 35(3):245–296
- Iverson RM (2015) Scaling and design of landslide and debris-flow experiments. *Geomorphology* 244:9–20
- Iverson RM, George DL (2014) A depth-averaged debris-flow model that includes the effects of evolving dilatancy. I. Physical basis. *Proc R Soc* 470(2170):20130819
- Jakob M, Hungr O (2005) *Debris-flow hazards and related phenomena*. Springer, Berlin
- Jiang YJ, Towhata I (2013) Experimental study of dry granular flow and impact behavior against a rigid retaining wall. *Rock Mech Rock Eng* 46:713–729
- Jiang YJ, Zhao Y, Towhata I, Liu DX (2015) Influence of particle characteristics on impact event of dry granular flow. *Powder Technol* 270:53–67
- Kang C (2016) Modelling entrainment in debris flow analysis for dry granular material. Ph.d. thesis. University of Alberta, Alberta, Canada
- Kanungo DP, Pain A, Sharma S (2013) Finite element modeling approach to assess the stability of debris and rock slopes: a case study from the Indian Himalayas. *Nat Hazards* 69(1):1–24
- Koo RCH, Kwan JSH, Ng CWW, Lam C, Choi CE, Song D, Pun WK (2016) Velocity attenuation of debris flows and a new momentum-based load model for rigid barriers. *Landslides* 14(2):617–629
- Kwan JSH (2012) Supplementary technical guidance on design of rigid debris-resisting barriers. Technical note no. TN 2/2012. Geotechnical Engineering Office, Civil Engineering and Development Department, The HKSAR Government
- Kwan JHS, Koo RCH, Ng CWW (2015) Landslide mobility analysis for design of multiple debris-resisting barriers. *Can Geotech J* 52(9):1345–1359
- Law RPH, Choi CE, Ng CWW (2015) Discrete element investigation of the influence of debris flow baffles on rigid barrier impact. *Can Geotech J* 53(2):179–185

- Leonardi A, Wittel FK, Mendoza M, Vetter R, Herrmann HJ (2014) Particle-fluid-structure interaction for debris flow impact on flexible barriers. *Comput-Aid Civil Infrastruct Eng* 31(5):323–333
- Leroy B (1985) Collision between two balls accompanied by deformation: a qualitative approach to Hertz's theory. *Am J Phys* 53(4):346–349
- Li X, He S, Luo Y, Wu Y (2010) Discrete element modeling of debris avalanche impact on retaining walls. *J Mt Sci* 7(3):276–281
- Lin DG, Hsu SY, Chang KT (2009) Numerical simulations of flow motion and deposition characteristics of granular debris flows. *Nat Hazards* 50(3):623–650
- Liu Z, Koyi HA (2013) Kinematics and internal deformation of granular slopes: insights from discrete element modelling. *Landslides* 10(2):139–160
- Mancarella D, Hungri O (2010) Analysis of run-up of granular avalanches against steep, adverse slopes and protective barriers. *Can Geotech J* 47(8):827–841
- McArdell BW, Bartelt P, Kowalski J (2007) Field observations of basal forces and fluid pore pressure in a debris flow. *Geophys Res Lett* 34(L07406):1–4
- Moriguchi S, Borja RI, Yashima A, Sawada K (2009) Estimating the impact force generated by granular flow on a rigid obstruction. *Acta Geotech* 4(1):57–71
- Ng CWW, Choi CE, Song D, Kwan JSH, Shiu HYK, Ho KKS, Koo RCH (2014) Physical modelling of baffles influence on landslide debris mobility. *Landslides* 12(1):1–18
- Ng CWW, Choi CE, Su AY, Kwan JSH, Lam C (2016) Large-scale successive impacts on a rigid barrier shielded by gabions. *Can Geotech J* 53(10):1688–1999
- Ng CWW, Song D, Choi CE, Kwan JSH, Shiu HYK, Koo RCH (2017a) Impact mechanisms of granular and viscous flows on rigid and flexible barriers. *Can Geotech J* 54(2):188–206
- Ng CWW, Choi CE, Goodwin RG, Cheung WW (2017b) Interaction between dry granular flow and deflectors. *Landslides* 14(1):1–11
- Ng CWW, Choi CE, Liu LHD, Wang Y, Song D, Yang N (2017c) Influence of particle size on the mechanism of dry granular run-up on a rigid barrier. *Geotech Lett* 7:1–11
- Podczeczek F, Mia Y (1996) The influence of particle size and shape on the angle of internal friction and the flow factor of unlubricated and lubricated powders. *Int J Pharm* 144(2):187–194
- Potyondy DO, Cundall PA (2004) A bonded-particle model for rock. *Int J Rock Mech Min Sci* 41:1329–1364
- Proske D, Suda J, Hübl J (2011) Debris flow impact estimation for breakers. *Georisk* 5(2):143–155
- Pudasaini SP, Hutter K (2007) *Avalanche dynamics*. Springer, Berlin, p 602
- Salciarini D, Tamagnini C, Conversini P (2010) Discrete element modeling of debris-avalanche impact on earthfill barriers. *Phys Chem Earth* 35(3):172–181
- Savage SB (1984) The mechanics of rapid granular flows. *Adv Appl Mech* 24:289–366
- Savage SB, Hutter K (1989) The motion of a finite mass of granular material down a rough incline. *J Fluid Mech* 199:177–215
- Song D, Ng CWW, Choi C, Zhou GG, Kwan JSH, Koo RCH (2017) Influence of debris flow solid fraction on rigid barrier impact. *Can Geotech J*. <https://doi.org/10.1139/cgj-2016-0502>
- Sovilla B, Schaer M, Kern M, Bartelt P (2008) Impact pressures and flow regimes in dense snow avalanches observed at the Vallée de la Sionne test site. *J Geophys Res Earth Surf* 113(F01010):1–14
- Speerli J, Hersperger R, Wendler C, Roth A (2010) Physical modeling of debris flow over flexible ring barriers. In: *Proceedings of 7th international conference of physical modelling in geotechnics, springman*. Laue and Seward, Taylor and Francis Group, London
- SWCB (2005) *Manual of soil and water conservation*. Soil and Water Conservation Bureau, Taiwan, 692 (in Chinese)
- Tan SB, Newton JM (1990) Powder flow ability as an indication of capsule filling performance. *Int J Pharm* 61(1–2):145–155
- Tang Y, Chan D, Zhu DZ (2017) A coupled discrete element model for the simulation of soil and water flow through an orifice. *Int J Numer Anal Meth Geomech*. <https://doi.org/10.1002/nag.2677>
- Teufelsbauer H, Wang Y, Chiou MC, Wu W (2009) Flow-obstacle interaction in rapid granular avalanches: DEM simulation and comparison with experiment. *Granular Matter* 11(4):209–220
- Teufelsbauer H, Wang Y, Pudasaini SP, Borja RI, Wu W (2011) DEM simulation of impact force exerted by granular flow on rigid structures. *Acta Geotech* 6:119–133
- Valentino R, Barla G, Montrasio L (2008) Experimental analysis and micromechanical modelling of dry granular flow and impacts in laboratory flume tests. *Rock Mech Rock Eng* 41(1):153–177
- VanDine DF (1996) *Debris flow control structures for forest engineering*. Ministry of Forests, British Columbia, p 68
- White DJ, Take WA, Bolton MD (2003) Soil deformation measurement using particle image velocimetry (PIV) and photogrammetry. *Geotechnique* 53(7):619–631

- Yuan R, Tang C, Deng Q (2015a) Effect of the acceleration component normal to the sliding surface on earthquake-induced landslide triggering. *Landslides* 12(2):335–344
- Yuan R, Tang C, Deng Q (2015b) Effect of the acceleration component normal to the sliding surface on earthquake-induced landslide triggering. *Landslides* 12:335–344
- Zanuttigh B, Lamberti A (2006) Experimental analysis of the impact of dry avalanches on structures and implication for debris flows. *J Hydraul Res* 47(4):381–383
- Zhang S, Hungr O, Slaymaker O (1996) The calculation of impact force of boulders in debris flow. *Debris flow observation and research*. Science Press, Beijing, pp 67–72
- Zhou GGD, Sun QC (2013) Three-dimensional numerical study on flow regimes of dry granular flows by DEM. *Powder Technol* 239:115–127
- Zhou JW, Cui P, Fang H (2013) Dynamic process analysis for the formation of Yangjiagou landslide-dammed lake triggered by the Wenchuan earthquake, China. *Landslides* 10(3):331–342
- Zhou JW, Huang KX, Shi C, Hao MH, Guo CX (2015) Discrete element modeling of the mass movement and loose material supplying the gully process of a debris avalanche in the Bayi Gully, Southwest China. *J Asian Earth Sci* 99:95–111